

Optical phonon modulation in semiconductors by surface acoustic wavesF. Iikawa,^{1,2} A. Hernández-Mínguez,¹ M. Ramsteiner,¹ and P. V. Santos^{1,*}¹*Paul-Drude-Institut für Festkörperelektronik, Hausvogteiplatz 5-7, 10117 Berlin, Germany*²*Instituto de Física “Gleb Wataghin”, Unicamp, 13083-859 Campinas-SP, Brazil*

(Received 8 January 2016; revised manuscript received 13 May 2016; published 31 May 2016)

We investigate the modulation of optical phonons in semiconductor crystals by a surface acoustic wave (SAW) propagating on the crystal surface. The SAW fields induce changes on the order of 10^{-3} in the time-averaged Raman peak intensity by optical phonons in Si and GaN crystals. The SAW-induced modifications in the intensity of the Raman lines are dominated by the modulation of the longitudinal optical (LO) phonon energy by the SAW strain field. We show that while the strain field of the excited Rayleigh SAWs changes the LO phonon energy, it does not mix it with the transversal optical modes. In addition to the previous contribution, which is of a local character, the experiments give evidence for a weaker and nonlocal contribution attributed to the spatial variation of the SAW strain field. The latter activates optical modes with large wave vectors and, therefore, lower energies. The experimental results, which are well described by theoretical models for the two contributions, prove that optical phonons can be manipulated by SAWs with μm wavelengths.

DOI: [10.1103/PhysRevB.93.195212](https://doi.org/10.1103/PhysRevB.93.195212)**I. INTRODUCTION**

Following the recent successful developments in photonics, phononics is presently attracting considerable attention and is establishing itself as a promising area for future science and technological applications. The conventional way of controlling phonons takes advantage of size confinement [1–3]. The advances in epitaxial crystal growth have made it possible to fabricate nanostructures with atomic dimensional control. These have been used to tailor the propagation properties of acoustic [4,5] and optical [6] phonons, as well as their interactions with optical fields [7,8].

One interesting question is whether optical phonons can also be controlled in a dynamic way by an external stimulus. To our knowledge, only a few approaches for the active control of optical phonons have so far been proposed. One example is the modulation of the optical modes in strongly piezoelectric materials by an acoustic wave [9]: Here, the anisotropic strain field created by a sub-MHz bulk acoustic wave has been shown to reduce the crystal symmetry, thus introducing changes in the Raman scattering from optical phonons.

In this paper, we demonstrate that surface acoustic waves (SAWs) provide a convenient tool for the dynamic manipulation of optical phonons in semiconducting materials. The SAWs used here are elastic surface vibrations in the GHz range, which are electrically excited on the semiconductor surface using interdigital transducers. Previous studies have addressed the modulation of photonic and electronic excitations in semiconductors by SAWs [10]. Here, we demonstrate that SAWs with wavelengths λ_{SAW} of a few μm can also modulate the Raman spectrum from optical phonons in Si and GaN crystals. For both materials, the changes in the peak intensity of the Raman lines are on the order of 0.1%. The strain field of a SAW can change the frequency and mix optical phonon modes. A systematic study shows that the SAW-induced modifications in the Raman peak intensity and line shape are due to two main mechanisms. The first is the periodic modulation of

the optical phonon energy by the SAW strain field [11]. The periodic phonon energy shifts are much smaller than the spectral width of the unperturbed Raman line and lead to an apparent reduction in peak intensity and broadening of the Raman line recorded in continuous-wave (cw) experiments. In addition to the previous contribution, which is of a local nature, the Raman experiments give evidence for a weaker and nonlocal contribution arising from the spatial variation of the SAW fields. The latter reduces the translation symmetry of the lattice, thus enabling scattering events that couple modes with different wave vectors. This mechanism activates modes with large wave vectors and, consequently, lower energies of the convex optical phonon dispersion of the crystal. The experimental Raman profiles are well reproduced by quantitative models for the two contributions. The results prove, therefore, the feasibility of optical phonons manipulation by SAWs with μm wavelengths.

In the remainder of this paper, we first describe the sample preparation and the experimental setup to record the changes in the Raman spectrum induced by SAWs. We then present experimental results obtained for both Si and GaN crystals. In a subsequent discussion section, we develop a theoretical model for the acoustic modulation and compare it to the experimental findings. The last section summarizes the main conclusions of this work.

II. EXPERIMENTAL DETAILS

The studies were carried out on high-resistivity, electronic quality (001) Si and (0001) GaN substrates containing interdigital transducers (IDTs) (cf. Fig. 1) for the excitation of SAWs fabricated by optical lithography. The split-finger IDTs were designed to launch SAWs with an acoustic wavelength $\lambda_{\text{SAW}} = 5.6 \mu\text{m}$ along a (110) ($(1\bar{1}20)$) surface direction of the Si (GaN) wafer, respectively. In the case of Si, SAW excitation was enabled by coating the substrates with a 300-nm-thick piezoelectric ZnO film produced by magnetron sputtering prior to the IDT deposition. The corresponding IDT resonance frequencies at room temperature are 746 and 1390 MHz for Si and GaN, respectively.

*santos@pdi-berlin.de

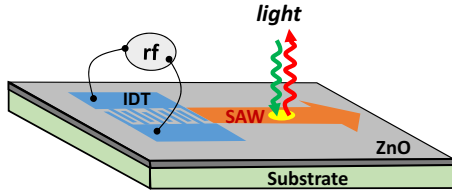


FIG. 1. Schematic diagram of a SAW delay line with interdigital transducers (IDT, only one IDT is shown) oriented along a $\langle 110 \rangle$ surface direction of a (001) silicon substrate coated with a piezoelectric ZnO thin film. The ZnO layer is absent in the GaN delay lines. The SAW propagation and incident and scattered light direction are shown.

The Raman scattering studies were performed in the backscattering configuration at room temperature using a confocal Horiba-LabRam system. The incident light from a 473 nm solid-state laser was focused onto a small spot (with a diameter of approximately $1 \mu\text{m} \ll \lambda_{\text{SAW}}$) on the sample surface by a $50\times$ long working distance objective with a numerical aperture (NA) of 0.55. The backscattered light was collected by the same objective, spectrally analyzed by a monochromator with a dispersion grating with 2400 grooves/mm, and detected using a liquid-nitrogen-cooled charge coupled device (CCD).

The changes in the Raman intensity induced by SAW are very small (on the order of 10^{-3}). Special precautions are thus required to discriminate the SAW-induced changes from variations arising from fluctuations in laser fluency and temperature (caused, for instance, by heating due to the application of a rf nominal peak power of typically 23 dBm to the IDT). For that purpose, we used a modulation detection scheme similar to the ones described in Ref. [9]. In this approach, both the excitation laser and the rf power for SAW generation were on/off chopped at a frequency of 617 Hz. Raman spectra $I_R(\omega)$ were then recorded with the light and rf modulation in phase (denoted as the *SAW-on* condition) and out-of-phase (*SAW-off* condition) with an integration time per measurement $t_m \sim 1$ min. The difference between these two spectra yields the changes induced by the SAW fields. In order to further reduce the effects of external fluctuations, the following periodic recording sequence with four steps per cycle i was used: $I_{\text{SAW,on}}^i(\omega)$, $I_{\text{SAW,off}}^{i+1}(\omega)$, $I_{\text{SAW,off}}^{i+2}(\omega)$, $I_{\text{SAW,on}}^{i+3}(\omega)$. This sequence was then repeated over $N \approx 60$ cycles, leading to a total accumulation time of typically 4 h. From the individual spectra we have determined the average Raman intensities in the SAW-on and SAW-off conditions, $I_{R,\text{on}}(\omega) = \frac{1}{4N} \sum_{i=1}^N (I_{\text{SAW,on}}^i + I_{\text{SAW,on}}^{i+3})$ and $I_{R,\text{off}}(\omega) = \frac{1}{4N} \sum_{i=1}^N (I_{\text{SAW,off}}^{i+1} + I_{\text{SAW,off}}^{i+2})$. From these two spectra, we then directly determined the total $I_R(\omega) = I_{R,\text{on}}(\omega) + I_{R,\text{off}}(\omega)$ and the differential Raman spectrum defined as $\Delta I_R(\omega) = I_{R,\text{on}}(\omega) - I_{R,\text{off}}(\omega)$ [12].

The modulation period $4t_m$ has been chosen to be short in comparison with the typical times for temperature and laser fluency fluctuations. As a result, $\Delta I_R(\omega)$ reflects the changes introduced by the SAW corrected for random fluctuations in temperature and laser fluency, which are linear in time. This data acquisition scheme, which proved to be essential for

obtaining reliable data over the total integration times, was automatically controlled by a computer program.

III. RESULTS

The bottom curves in Figs. 2(a) and 2(b) display normalized backscattering Raman spectra for Si and GaN recorded in the absence of a SAW, respectively. The Si Raman spectrum is characterized by a single peak at 521.2 cm^{-1} associated with longitudinal optical (LO) phonons and possessing with a full width at half maximum (FWHM) of 3.0 cm^{-1} . This linewidth, which is significantly larger than the spectral resolution of 0.5 cm^{-1} , attests to the high crystal quality of sample. The Raman spectra from the ZnO-coated Si sample also display the Raman lines from the ZnO overlayer. However, we were not able to detect SAW-induced changes in these lines, probably due to the fact that their Raman intensities were much lower than the one for the Si line.

The investigated GaN line at 570.0 cm^{-1} is associated with the excitation of the E_2^h mode [13,14]. GaN has also a second Raman-active $A_1(\text{LO})$ mode at 735.5 cm^{-1} : Its intensity, however, is lower than the one for the E_2^h mode. Due to the worse signal-to-noise ratio, SAW modulation studies have not been carried out for the 735.5 cm^{-1} mode.

The additional curves in the panels of Fig. 2 show differential Raman spectra $\Delta I_R(\omega)$ obtained using the modulation technique described above for different SAW frequency shifts Δf_{SAW} relative to the IDT resonance frequency f_{SAW} . In each panel, the spectra have been normalized to the maximum value $I_{R,\text{max}}$ of the $I_R(\omega)$ spectrum recorded at f_{SAW} . The maximum modulation amplitude reaches 0.5% and 0.8% of $I_{R,\text{max}}$ for Si and GaN, respectively, and reduces when the excitation frequency shifts away from f_{SAW} .

The differential Raman spectra $\Delta I_R(\omega)$ in Fig. 2 are characterized by a pronounced negative dip at the central Raman frequency with asymmetric flanks around this frequency, which indicates a preferential transfer of oscillator strength towards lower Raman shifts. In order to extract quantitative information from the differential spectra in Figs. 2(a) and 2(b), we fit each $\Delta I_R(\omega)$ spectrum to the function [15]

$$f(\omega) = \text{Re} \left\{ \frac{Ae^{i\theta}}{(\omega - \omega_0 + i\gamma)^2} \right\}, \quad (1)$$

where A , θ , ω_0 , and γ denote the amplitude, phase, resonance frequency, and spectral broadening, respectively. This function is similar to the one used to analyze the line shape of modulation spectroscopy signals, including electroreflectance and low frequency (hundreds of Hz) piezoreflectance line shapes [16].

The solid lines superimposed on the experimental data in Fig. 2 were obtained by fitting Eq. (1) to the measured spectra. For small detuning (i.e., $\Delta f_{\text{SAW}} < 0.5$ MHz), the fits to the Si data yield $\theta = 0.8 \pm 0.1$ rad and $\gamma = 1 \pm 0.1 \text{ cm}^{-1}$. γ is comparable to the half width of the Raman line and, as will be shown later, much larger than the SAW-induced shifts of the phonon energies. For large detunings, reliable values for θ and γ could not be determined due the low amplitude of the differential Raman signal. In this case, the fittings were carried out by fixing θ and γ to the values at $\Delta f_{\text{SAW}} = 0$ and only varying the amplitude A . The symbols in

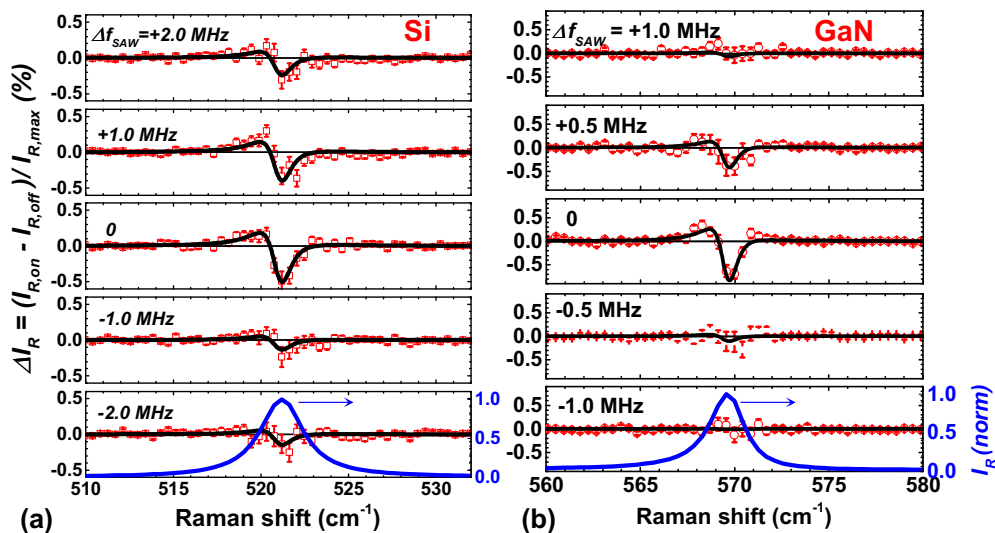


FIG. 2. Normalized total $I_R(\omega)$ and differential $\Delta I_R(\omega)$ Raman spectra for (a) Si and (b) GaN recorded for different rf frequency shifts Δf_{SAW} relative to the IDT resonance frequency f_{SAW} . Each spectrum is normalized to its maximum value. The resonance frequency f_{SAW} is equal to 746 MHz and 1.39 GHz for Si and GaN, respectively, and the resonance band is approximately 1 MHz wide (cf. s_{11} plots in Fig. 3). The error bars were obtained from the statistical analysis of the Raman spectra ensemble (see text for detail). The solid lines obtained from the fits of Eq. (1) to the experimental data are also shown.

Figs. 3(a) and 3(b) show for Si and GaN, respectively, the fitted amplitudes A as a function of the rf frequency applied to the IDT. The solid lines reproduce, for comparison, the frequency dependence of the rf reflectivity of the IDT (corresponding to the rf scattering parameter s_{11}) with the characteristic dip within the frequency band for SAW generation. The maximum of A is within the resonance frequency range of the IDT and its spectral dependence follows the one for the SAW generation efficiency.

In the case of Si, while $\Delta I_R(\omega)$ reduces considerably away from f_{SAW} , it does not vanish completely since the measured range of frequencies is not sufficiently far away from the emission band of the IDT. Since the Raman measurements were carried out very close to the IDT (approximately 50 μm away), the residual signal may also be due to the excitation of other (non-SAW) acoustic modes by the IDT. Nevertheless,

the results in Figs. 3(a) and 3(b) confirm that the changes in the Raman spectra are due to the SAW strain field.

Finally, in order to prove that the spectral changes only occur within the SAW beam, we have recorded differential Raman spectra at different positions on the sample surface. Figures 4(a) and 4(c) compare results for Si and GaN, respectively, obtained on the positions P_1 – P_4 indicated in Fig. 4(b). P_3 and P_4 are outside and P_1 and P_2 are within the 100- μm -wide SAW beam (the beam width is determined by the aperture of the IDT; cf. Fig. 1). All measurement spots are located 50 μm away for the IDT and separated by 50 μm . Note that a clear differential signal is only observed for the positions within the SAW beams. Furthermore, the temperature at all spots due to SAW excitation should be approximately the same since their separation is much smaller than the dimensions of the IDT. The different line shapes and the smaller amplitudes

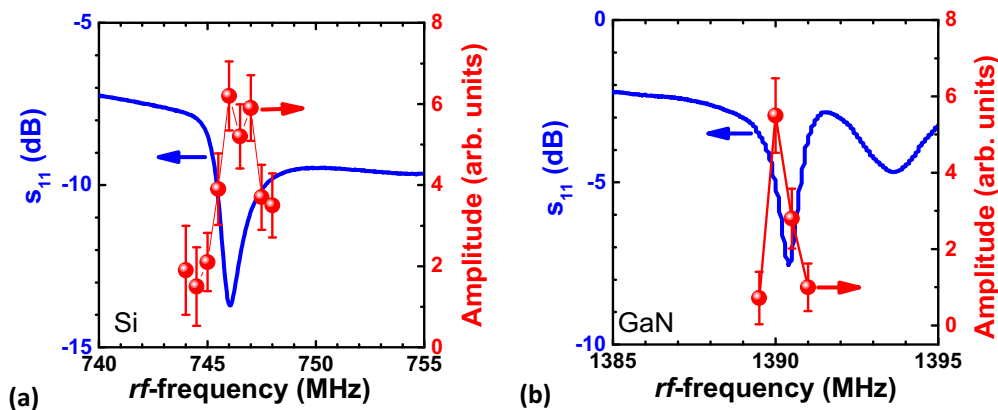


FIG. 3. The rf reflectivity of the IDT (corresponding to the scattering parameter s_{11} , solid line) and fitting amplitudes A (symbols) extracted from the curves of Fig. 2 to Eq. (1) (see text for details).

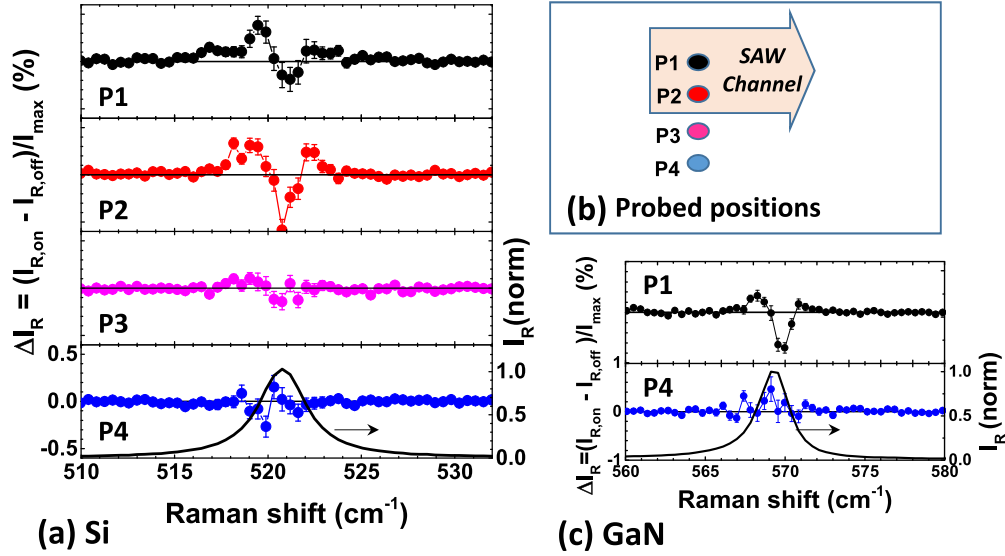


FIG. 4. Differential Raman spectra for (a) Si and (c) GaN recorded at the positions P_1 – P_4 indicated in (b). P_1 and P_2 are within and P_3 and P_4 outside the 100- μm -wide SAW beam (adjacent points are separated by 50 μm).

of the signals recorded at P_3 and P_4 in comparison with those at P_1 and P_2 thus prove that the differential technique described in the previous section effectively discriminates the effects of the SAW fields.

IV. DISCUSSION

In this section, we will first present a detailed analysis of the results obtained for silicon and then discuss the applicability of similar concepts for GaN.

The zone-center optical modes in Si consist of one longitudinal (LO) and two transverse (TO) modes. In the absence of a SAW, these three modes are degenerate, but only the LO mode is Raman active in the backscattering configuration from the (001) surface. The phonon mode involved in the scattering propagates perpendicularly to the surface with wave vector $q_z \hat{e}_z = \frac{4\pi\tilde{n}}{\lambda_f} \hat{e}_z$ and energy given by the phonon dispersion $\omega(q_z \hat{e}_z)$. In these expressions, \tilde{n} is the refractive index and \hat{e}_z the unitary vector along the surface normal, which corresponds to the z direction.

The acoustic field introduces a periodic time and spatial modulation of the optical phonon energies as well as of the dielectric properties of the medium. Since the SAW frequency is much smaller than the optical frequencies, we can safely assume that the optical phonon frequencies adiabatically follow the acoustic modulation. The acoustic modulation affects the spectral shape of the differential Raman spectra in two different ways. First, the strain field periodically modulates the optical phonon energies. Since the energetic shifts are much smaller than the spectral width of the Raman line, the main effect in the time-integrated Raman spectrum is to transfer oscillator strength from the center to the flanks of the line. This mechanism is expected to produce a symmetric differential Raman spectrum with a negative dip at the Raman central frequency and positive values at the flanks, in agreement with the line shape of Eq. (1) for $\theta = 0$.

This line shape qualitatively reproduces the main features of the data in Figs. 2 and 4.

In addition to the symmetric contribution described above, the differential Raman spectra also show an asymmetric contribution yielding a stronger intensity at low Raman shifts. The spatially resolved plots of Fig. 4 show that this contribution cannot be explained by changes in temperature induced by SAW excitation. We attribute this contribution to phonon scattering processes arising from the spatial modulation of the refractive index and phonon energies by the SAW field. This nonlocal mechanism reduces the crystal translation invariance symmetry and induces (i) a mixing of the TO and LO modes of the undisturbed crystal and (ii) the coupling of dispersion modes $\omega(\mathbf{q})$ with different \mathbf{q} 's. Due to the negative curvature of the optical phonon dispersion, mechanism (ii) transfers oscillator strength from the high to the low frequency flank of the Raman line, thus leading to an asymmetric contribution to $\Delta I_R(\omega)$. Such a process has been invoked to account for the Raman line shape for nanocrystals [1,2]. A similar behavior is also observed in Fig. 2 and can be reproduced by setting $\theta = \pi/2$ in Eq. (1).

The combination of the mechanisms described above qualitatively reproduces the spectral shape of the $\Delta I_R(\omega)$ curves in Fig. 2. In the following sections, we proceed to a quantitative analysis of the impact of these mechanisms together with a comparison with the experimental results.

A. Acoustic field distribution

The strain field ε of a Rayleigh SAW propagating along the x' ||[110] direction of the surface contains three nonvanishing components and can be expressed (in the Voigt notation) as $\varepsilon = (u_{x'x'}, 0, u_{zz}, 0, u_{x'z}, 0)$. Here, u_i ($i = x' || [110], y' || [\bar{1}10], z || [001]$) are the displacement and u_{ij} the associated strain components [10]. The spatial distribution of the strain field was obtained from an elastic continuum calculation of the SAW modes in the structure of Fig. 1

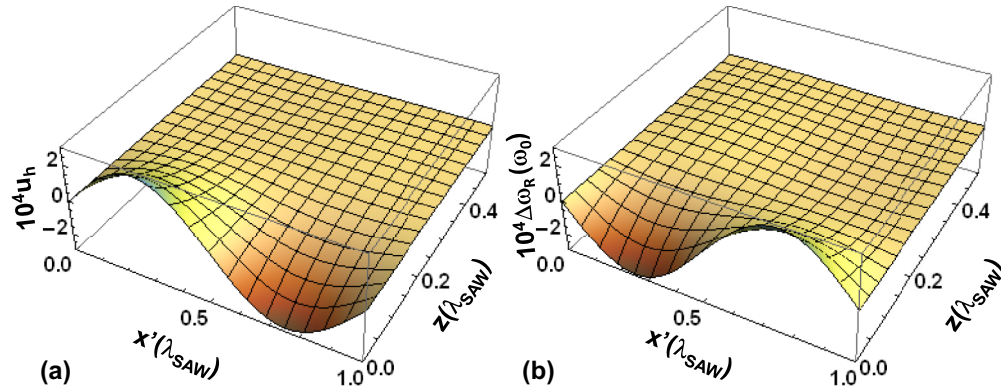


FIG. 5. Spatial distribution of the (a) hydrostatic strain $u_h = u'_{x'x'} + u_{zz}$ and (b) local phonon frequency shifts $\Delta\omega_R$ induced by a SAW with a wavelength $\lambda_{\text{SAW}} = 5.6 \mu\text{m}$ propagating along the $x' = [110]$ direction of the ZnO/Si structure (see Fig. 1). Note that $z = 0$ corresponds to the coordinate of the ZnO/Si interface.

following the procedure described in Ref. [10]. These calculations take into account the presence of the ZnO layer on top of the Si substrate. Results for the hydrostatic component $u_h = u'_{x'x'} + u_{zz}$ induced by a SAW with wavelength $\lambda_{\text{SAW}} = 5.6 \mu\text{m}$ and linear power density (e.g., the ratio between the acoustic power and the SAW beam width) of 76 W/m are shown in Fig. 5(a) (this acoustic power density corresponds to the maximum value that can be generated by the transducers without considerably increasing the sample temperature). In the plots of Fig. 5, the ZnO/Si interface is at $z = 0$ and the Si substrates fill the $z > 0$ half plane. The calculation conditions correspond to the ones in Fig. 2(a) with the IDT excited at its resonance frequency. The absolute values for the strain components were obtained from the electric power coupled to

the acoustic mode determined from the rf reflection coefficient s_{11} (cf. Fig. 3).

B. Phonon frequencies

Backscattering Raman experiments on (001) Si surfaces can, in principle, probe the longitudinal (LO) and the two transverse (TO) optical modes with small wave vector along the z direction. In the absence of a SAW, the three zone-center modes are degenerate with frequency ω_0 and only the LO mode contributes to the Raman signal. The SAW strain field may mix these modes and lift their degeneracy. In the basis defined by the vectors (x' , y' , and z) defined above, the phonon frequencies ω under a SAW can be written as $\omega^2 - \omega_0^2 = \lambda_0$, where λ_0 are the eigenvalues of the secular matrix

$$M_{\text{ph}} = \begin{pmatrix} [pu'_{x'x'} + q(u'_{x'x'} + 2u_{zz})]/4 & ru'_{x'x'} & 0 \\ ru'_{x'x'} & [pu'_{x'x'} + q(u'_{x'x'} + 2u_{zz})]/4 & 0 \\ 0 & 0 & pu_{zz} + qu'_{x'x'} \end{pmatrix}. \quad (2)$$

This expression was obtained by a coordinate transformation of the secular equation for the (x, y, z) basis defined in Ref. [17]. Here, p , q , and r denote the phonon deformation potentials with experimental values for Si given by [11] $p/\omega_0^2 = -1.85$, $q/\omega_0^2 = -2.30$, and $r/\omega_0^2 = -0.71$. For the small strain levels induced by the SAW modulation, the phonon frequency shifts are much smaller than the linewidth of the LO Raman line. Under this condition, the Raman shift $\Delta\omega_R = \omega - \omega_0$ becomes $\Delta\omega_R \approx +\frac{\lambda_0}{2\omega_0}$.

The solution of Eq. (2) for the SAW strain field distribution in Fig. 5(a) yields, at each spatial/time position, three eigenmodes $\lambda_{0,i}$ ($i = 1, 3$) as well as three associated eigenvectors ϕ_i . The upper 2×2 diagonal block of Eq. (2) shows that two of these eigenmodes are of transverse character and result from the mixing of the unperturbed TO modes. A remarkable consequence of Eq. (2) is that, despite the complexity of the SAW strain field, it does not modify the symmetry of the z -polarized mode (corresponding to the LO phonon mode). Although the frequency of this mode shifts, its Raman cross section remains equal to the one in the unperturbed crystal.

Furthermore, since only the TO modes are not Raman active in the backscattering geometry, only the LO frequency variations need to be considered in the determination of the differential Raman spectrum. Figure 5(b) compares the spatial distribution of $\Delta\omega_R$ for the LO mode with the hydrostatic strain profile [Fig. 5(a)]. $\Delta\omega_R$ closely resembles the hydrostatic strain distribution with largest amplitudes close to the $z = 0$ (i.e., close to the ZnO/Si interface) and positive frequency shifts at the location of compressive strain (i.e., $u_h < 0$).

C. Differential Raman spectrum

In order to determine the modifications in the Raman spectrum induced by the acoustic field, we will assume that the optical phonons can be considered as particles with an effective mass given by the LO dispersion subjected to an effective phonon potential $\Delta\omega_R$ given by Fig. 5(b). The components of the Fourier transform of this potential profile act as interaction potentials for phonons with different wave vectors \mathbf{q} and, consequently, different energies given by the wave vector

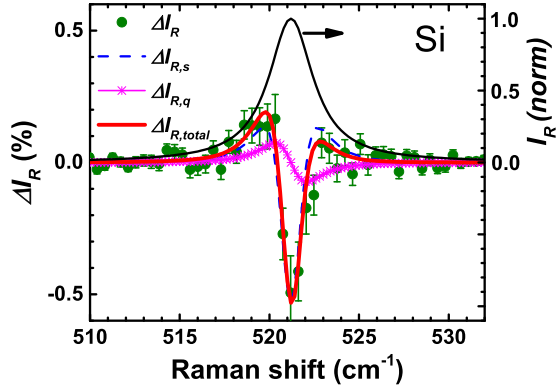


FIG. 6. Experimental and calculated differential Raman intensity of Si by taking into account only the strain-induced frequency modulation $\Delta I_{R,s}$, only the coupling between states with different \mathbf{q} vectors $\Delta I_{R,q}$, and total contribution $\Delta I_{R,total}$. I_R shows, for comparison, the unperturbed Raman spectrum.

dependence of the phonon dispersion $\omega(\mathbf{q})$. In this way, one can set up an eigenvalue equation yielding the phonon modes under the SAW potential. The solution of this equation gives the phonon states of the perturbed system.

Instead of solving the full eigenvalue problem, we examine here two limiting approximations determined by the phonon coherence length ℓ_{ph} . The latter is an important parameter governing the phonon properties in the modulated potential, since it determines the region over which the vibrational modes average the local potential variations displayed in Fig. 5(b). First, we consider the situation where $\ell_{\text{ph}} \ll \lambda_{\text{SAW}}$, which is expected to hold here since λ_{SAW} is much larger than the lattice period. In this case, the Raman spectrum becomes proportional to the phonon density of states in the potential landscape of Fig. 5(a), which can be obtained by simply integrating the frequency-shifted contributions over the scattering volume. For Si, the short optical penetration depth (which corresponds to only 5% of λ_{SAW}) allows for a further simplification, since the differential Raman contribution $\Delta I_{R,s}(\omega)$ can be obtained by a one-dimensional integration along x' for $z = 0$ according to

$$\Delta I_{R,s}(\omega) = \frac{1}{\lambda_{\text{SAW}}} \int_0^{\lambda_{\text{SAW}}} I_{R,0}[\omega, \omega_0 + \Delta\omega_R(x', 0)] dx' - I_{R,0}(\omega, \omega_0). \quad (3)$$

Here, $I_{R,0}(\omega, \omega_0)$ denotes the spectral shape of the unperturbed Raman intensity with the Raman line at ω_0 . The latter will be assumed to be a Lorentzian function with linewidth corresponding to the measured value of 3.0 cm^{-1} .

The calculated $\Delta I_{R,s}$ displayed in Fig. 6 reproduces well the amplitude and spectral shape of the main dip observed in the measured differential Raman spectrum (symbols). The amplitude of the oscillation in the phonon frequency corresponds in this case to 0.16 cm^{-1} , which is equal to approximately 10% of the half width of the Raman line.

While the previous model reproduces well most of the experimental features, it cannot account for the slightly asymmetric shape of the differential spectrum with respect to the center frequency, which is particularly strong for Si (cf. Fig. 2). The natural mechanism to account for the asymmetry

is the coupling of modes with different \mathbf{q} 's induced by the acoustic modulation. Such a contribution is expected if the coherence length ℓ_{ph} becomes comparable to the spatial extent of the modulation potential created by the SAW. Under these conditions, the Fourier component $\mathcal{F}_{\text{ph}}(\Delta\mathbf{q})$ will couple modes with wave vectors differing by $\Delta\mathbf{q}$. Due to the parabolic shape of the phonon dispersion close to the zone center $\omega(\mathbf{q}) = \omega(0) - (\mathbf{q})^T \mathbf{a}(\mathbf{q})$, where $\omega(0) = \omega(\mathbf{q} = \mathbf{0})$ and \mathbf{a} describes the curvature of the LO dispersion, the strongest contribution to the scattering comes from the large scattering vectors. According to Fig. 5, these are found for $\Delta\mathbf{q} \parallel z$ as a consequence of the strong decay of the acoustic field with depth.

We will estimate the contribution $\Delta I_{R,q}(\omega)$ from the $\Delta\mathbf{q}$ coupling to the differential intensity using the phenomenological approach developed for nanocrystals by Campbell and Fauchet [2]. The latter assumes that the Raman spectrum involves contributions of \mathbf{q} vectors around the Γ point with a characteristic cutoff wave vector q_{max} , thus leading to a differential spectrum $\Delta I_{R,q}(\omega)$ given by

$$\Delta I_{R,q}(\omega) = \frac{1}{q_{\text{max}} \sqrt{2\pi}} \int_{-\infty}^{\infty} I_{R,0}[\omega, \omega(q)] \times \exp \left[- \left(\frac{q}{q_{\text{max}} \sqrt{2}} \right)^2 \right] dq - I_{R,0}(\omega, \omega_0). \quad (4)$$

The differential intensity $\Delta I_{R,q}(\omega)$ calculated for $q_{\text{max}} = 40k_{\text{SAW}}$, which is shown by the crosses in Fig. 6, has an antisymmetric, S-like line shape similar to the one observed in the experimental data. Furthermore, the calculated total differential spectrum $\Delta I_{R,total}(\omega) = \Delta I_{R,s}(\omega) + \Delta I_{R,q}(\omega)$ reproduces very well the experimental line shapes over the whole range of Raman shifts, as displayed by the thick solid line in Fig. 6.

The model for the $\Delta I_{R,q}(\omega)$ contribution requires large values for q_{max} ($q_{\text{max}} \gg k_{\text{SAW}} = 2\pi/\lambda_{\text{SAW}}$) to reproduce the experimental results, thus implying the existence of nonvanishing Fourier components up to the 40th order. According to the phonon potential profiles (cf. Fig. 5), the highest Fourier coefficients arise from the decay of the SAW amplitude with depth (rather than from the variation along the SAW propagation direction). The latter, however, leads to nonvanishing Fourier components only up to approximately $10k_{\text{SAW}}$. The generation of phonons with large wave vectors must, therefore, proceed via multiscattering events. Further studies will be required to elucidate the origin of this strong nonlocal contribution.

D. Analysis of the GaN data

Calculations similar to those described above can in principle also be carried out to determine the strain-induced changes in frequency and mixing of modes for GaN. There are, however, important differences relative to Si. The LO and TO zone-center optical modes are not degenerate in this polar material. Equation (2) needs, therefore, to be modified to account for the different symmetry of the wurtzite lattice as well as for the energetic LO-TO splitting and its dependence on the SAW fields. In addition, the experimental phonon dispersion for the E_2^h mode is not well known [18], thus leading to uncertainties in the analysis. Finally, since the GaN substrate is transparent for the used laser line, the Raman experiments

probe a sample depth larger than the SAW decay length, thus making a quantitative analysis more difficult than for Si. The analysis of the GaN results requires, therefore, more elaborate calculations, which are out of the scope of the present paper. Nevertheless, the asymmetric line shape observed in GaN, shown in Fig. 2(b), similar to the Si, is an indirect indication of the negative dispersion of the E_2^h phonon mode predicted by *ab initio* calculations [13,18,19].

V. CONCLUSIONS

We demonstrate that surface acoustic waves can modulate optical phonons in Si and GaN semiconductors. The SAW-induced variation in the peak intensity of the Raman lines, which is of the order of 10^{-3} , shows characteristic features attributed to two effects. The main contribution is identified as the modulation of the LO phonon frequency by the SAW strain. Interestingly, while the strain field of the Rayleigh SAWs used here changes the LO phonon energy, it does not mix

it with transverse modes. The second effect is the coupling of the phonon wave vectors induced by the nonhomogeneous distribution of the SAW fields. The latter is of nonlocal origin and associated with the short-range spatial variations of the SAW fields. The differential Raman intensity calculated using a model that includes both contributions is in good agreement with the experimental spectra. Future studies should address procedures to increase the SAW-induced frequency shift of the optical modes. A straightforward mechanism is the increase of the density power density, which can be achieved via the use of focusing transducers [20] and or SAW resonators [21,22].

ACKNOWLEDGMENTS

We thank V. Kaganer for discussions and for a careful reading of the manuscript. F.I. acknowledges financial support from the Alexander von Humboldt-Stiftung (Germany), Fundação de Amparo à Pesquisa do Estado de São Paulo (FAPESP, Brazil), and Conselho Nacional de Desenvolvimento Científico e Tecnológico (CnPq, Brazil).

-
- [1] H. Richter, Z. P. Wand, and L. Ley, *Solid State Commun.* **39**, 625 (1981).
- [2] I. Campbell and P. Fauchet, *Solid State Commun.* **58**, 739 (1986).
- [3] U. Woggon, F. Gindele, O. Wind, and C. Klingshirn, *Phys. Rev. B* **54**, 1506 (1996).
- [4] V. Narayanamurti, H. L. Störmer, M. A. Chin, A. C. Gossard, and W. Wiegmann, *Phys. Rev. Lett.* **43**, 2012 (1979).
- [5] B. Jusserand, D. Paquet, and A. Regreny, *Phys. Rev. B* **30**, 6245 (1984).
- [6] A. K. Sood, J. Menéndez, M. Cardona, and K. Ploog, *Phys. Rev. Lett.* **54**, 2111 (1985).
- [7] A. Fainstein, B. Jusserand, and V. Thierry-Mieg, *Phys. Rev. Lett.* **75**, 3764 (1995).
- [8] N. D. Lanzillotti-Kimura, A. Fainstein, C. A. Balseiro, and B. Jusserand, *Phys. Rev. B* **75**, 024301 (2007).
- [9] A. N. Vtyurin, A. D. Schafer, and A. S. Krylov, *Ferroelectrics* **170**, 181 (1995).
- [10] M. M. de Lima, Jr. and P. V. Santos, *Rep. Prog. Phys.* **68**, 1639 (2005).
- [11] E. Anastassakis, A. Cantarero, and M. Cardona, *Phys. Rev. B* **41**, 7529 (1990).
- [12] One may argue that the four-cycle sequence can also be viewed as ON(OFF-OFF-ON-ON-OFF-OFF-ON-ON OFF-OFF-ON-ON)-OFF, where the part within the parentheses is a two-cycle sequence. If the number of steps N is much larger than $1/r_R$, where r_R is the relative change in intensity induce by the SAW, then there would be no significant differences between the two- and the four-step sequences. In our case, however, $N \approx 1/r_R$, so that the contributions of the two steps outside the parentheses remain relevant.
- [13] H. Siegle, G. Kaczmarczyk, L. Filippidis, A. P. Litvinchuk, A. Hoffmann, and C. Thomsen, *Phys. Rev. B* **55**, 7000 (1997).
- [14] V. Y. Davydov, Y. E. Kitaev, I. N. Goncharuk, A. N. Smirnov, J. Graul, O. Semchinova, D. Uffmann, M. B. Smirnov, A. P. Mirgorodsky, and R. A. Evarestov, *Phys. Rev. B* **58**, 12899 (1998).
- [15] D. A. Aspnes and A. A. Studna, *Phys. Rev. B* **7**, 4605 (1973).
- [16] A. Gavini and M. Cardona, *Phys. Rev. B* **1**, 672 (1970).
- [17] F. Cerdeira, C. J. Buchenauer, F. H. Pollak, and M. Cardona, *Phys. Rev. B* **5**, 580 (1972).
- [18] T. Ruf, J. Serrano, M. Cardona, P. Pavone, M. Pabst, M. Krisch, M. D'Astuto, T. Suski, I. Grzegory, and M. Leszczynski, *Phys. Rev. Lett.* **86**, 906 (2001).
- [19] C. Bungaro, K. Rapcewicz, and J. Bernholc, *Phys. Rev. B* **61**, 6720 (2000).
- [20] M. M. de Lima, Jr., F. Alsina, W. Seidel, and P. V. Santos, *J. Appl. Phys.* **94**, 7848 (2003).
- [21] D. L. T. Bell and R. C. M. Li, *Proc. IEEE* **64**, 711 (1976).
- [22] M. M. de Lima, Jr., P. V. Santos, Y. A. Kosevich, and A. Cantarero, *Appl. Phys. Lett.* **100**, 261904 (2012).